Topology-protected displacement metrology using broadband unpolarized light

Di Liu,[1,*] Han Liu,[1,*] H.P. Urbach,[2] and Zheng Xi[1,†]

[1] *Department of Optics and Optical Engineering, School of Physical Sciences, University of Science and Technology of China, Hefei, Anhui 230026, People's Republic of China*

[2] *Department of Imaging Physics, Optica Research Group, Delft University of Technology, Lorentzweg 1, 2628 CJ Delft, The Netherlands*

(Received 8 July 2024; revised 26 July 2025; accepted 28 October 2025; published 14 November 2025)

We introduce topological invariants into displacement metrology and show that robust topological structures in momentum space can be used to retrieve the displacement of a small particle. Owing to its topological nature, the proposed scheme is general. It does not require phase or polarization stability and works even under broadband unpolarized illumination with randomly fluctuating phases. Remarkably, unpolarized illumination can achieve a superior performance to its coherent counterpart, owing to closely packed in-plane polarization singularity structures with very high displacement sensitivities nearby. Our work opens an avenue for developing topologically protected ultrasensitive metrological methods with randomly fluctuating fields.

DOI: 10.1103/q77s-h3wg

I. INTRODUCTION

The precise measurement of small displacements serves as a driving force behind modern science and technology [1–6]. To date, many innovations have emerged, from large-scale interferometers [7] with high-finesse cavities [8] and novel quantum states of light [9] to miniaturized systems using structured light [6,10] and its interactions with resonant nanoparticles [11–13]. Despite various forms, the core is to encode small displacements into sensitive phase shifts of light that can be measured interferometrically. Thus, phase or polarization stability is crucial, especially for schemes using structured light. Random phase or polarization fluctuations known as decoherence or depolarization can cause noise, reducing the contrast and sensitivity.

Topology is the study of invariant properties under continuous deformation [14]. Owing to its robustness, it has shown great potential in implementing noise-resilient systems such as topological insulators and photonics [15–20]. This leads to an interesting question. Can displacement metrology benefit from topological robustness? Specifically, can topology be used to overcome noises such as decoherence and depolarization while maintaining high sensitivity?

In this work, we introduce topological protection into displacement metrology and propose a scheme to measure the displacement of a small particle placed inside a focused field by tracking its momentum-space topological singularities. Owing to its topological nature, the scheme even works under broadband unpolarized illumination with randomly fluctuating phases. Surprisingly, under unpolarized illumination, which is often treated as noise because of a loss of coherence, the uncorrelated field components can create tightly packed points of in-plane polarization singularities with very high displacement sensitivity nearby. These points are spaced well below the diffraction limit, within one Airy disk, owing to incoherence, creating a broader range of high sensitivity than polarized illumination. These hidden aspects of unpolarized illumination are particularly interesting for metrological applications. Our work opens up new possibilities for ultrasensitive metrological methods using randomly fluctuating fields.

II. RESULTS

A. Working principle and geometric interpretation

The system under study is shown in Fig. 1(a). We want to retrieve a particle's transverse displacement inside a focal field. Our starting point is the topological invariant in momentum space, i.e., on the far-field sphere S^2. According to the Poincaré-Hopf theorem, one can construct a tangential vector field or a line field on S^2, and the index sum of the singularities of this field should equal $+2$ (Euler characteristic) [21,22]. This number is the topological invariant of the sphere S^2 and remains unchanged, even under randomly fluctuating illumination.

To see this, let us consider an unpolarized quasimonochromatic illumination of central frequency ω and

*These authors contributed equally.
†Contact author: zheng.xi@ustc.edu.cn

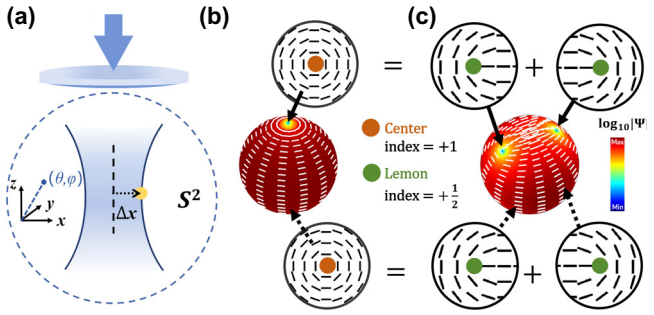

FIG. 1. (a) Light is focused through a lens (numerical aperture = 0.95) onto a particle to retrieve its displacement. (b) Distribution of the polarization line field (white lines) and $\log_{10}|\Psi|$ (colored background) on S^2 when the particle is at $x = 0$ under unpolarized illumination. The top and bottom insets give enlarged views around the singularities at the north and south poles, respectively. The dashed arrow points to the singularity at the south pole that is not visible in this plot. (c) As (b), except that the particle is at $x = 0.2\lambda$. Note that the splitting of singularities is along the x-axis and S^2 is rotated for better visualization.

wavelength λ. It consists of equal amounts of x- and y-polarized light with randomly fluctuating phases [23–25]. Rotating polarizers can be used to measure the local polarization direction of the scattered field on S^2 [26], which constitutes the line field in Fig. 1(b). When the scattered field at one point on S^2 is unpolarized, circularly polarized, or a mixture of both, its polarization direction is undefined and the line field becomes a singularity, around which an index can be assigned [22,27]. These singularities also correspond to the 0s of the Stokes field $\Psi = s_1 + is_2$ [28] with $s_1 = s_2 = 0$, where s_1 and s_2 are the two Stokes parameters.

In Fig. 1(b), we plot the distribution of the line field and $\log_{10}|\Psi|$ on S^2 when the particle is at the focal point, with $x = 0$. There are two center-type singularities of index $+1$ at the north and south poles, so the total index on S^2 is $+2$. These index $+1$ singularities are unstable. When the particle is displaced by $\Delta x = 0.2\lambda$, as shown in Fig. 1(c), each of the two center-type singularities splits into two lemon-type singularities of index $+1/2$. The total index on S^2 remains $+2$, as required.

The existence of these singularities is protected by the topological invariant of the momentum sphere. Their locations can be used to infer Δx. The advantage is clear: Unlike interferometric schemes that rely heavily on light sources with stable phase or polarization, this scheme works under any illumination.

To understand the nature and dynamics of the singularities, we follow previous works [23,29,30] and use the polarization matrix $\Phi = \langle \vec{E}^* \vec{E}^T \rangle$ to describe the system. The matrix element $\Phi_{ij} = \langle E_i^* E_j \rangle$ represents the correlation between the electric field components E_i and E_j, with the brackets denoting the ensemble average. For convenience, we take $i,j = x,y$ at the entrance pupil; $i,j = \theta,\phi$ on the momentum sphere S^2; and $i,j = x,y,z$ in the focal region.

The polarization matrix for the scattered field can be expressed as $\Phi_s = \frac{1}{2}\sum_{i=0}^{3} s_i \sigma_i$ [23], where s_i are the Stokes parameters and σ_i are the Pauli spin matrices. Because σ_3 is imaginary, the singularities ($s_1 = s_2 = 0$) correspond to points on S^2 with

$$\Re\{\Phi_s(\theta,\phi)\} = \frac{1}{2} s_0 \sigma_0 = \frac{1}{2} s_0 I. \tag{1}$$

In essence, $\Re\{\Phi_s(\theta,\phi)\}$ is a two-dimensional real and symmetric tensor. The eigenvector corresponding to its largest eigenvalue determines the direction of the polarization line field shown in Fig. 1 [22]. Along specific angles, $\Re\{\Phi_s(\theta,\phi)\}$ is proportional to the identity matrix I, with identical eigenvalues. These directions correspond to the singularities.

A small and isotropic particle can be approximated as a point dipole with a scalar polarizability, and $\Re\{\Phi_s(\theta,\phi)\}$ can be obtained using the Green's function theory [30] (see the Supplemental Material [32] for a detailed derivation):

$$\Re\{\Phi_s(\theta,\phi)\} = D_0 \mathcal{P}(\theta,\phi) \Re\{\Phi_f(x,y,z)\} \mathcal{P}(\theta,\phi)^T, \tag{2}$$

where $\Phi_f(x,y,z) = \langle \vec{E}_f^* \vec{E}_f^T \rangle$ is the 3×3 polarization matrix for the focal field $\vec{E}_f = [E_{f,x}, E_{f,y}, E_{f,z}]^T$ at the particle's position, $D_0 = k^4 |\alpha|^2 / 16\pi^2 r^2 \epsilon_0^2$ is a scaling factor containing the wavenumber k and the polarizability α, and $\mathcal{P}(\theta,\phi) = \hat{\theta}\hat{\theta}^T + \hat{\phi}\hat{\phi}^T$ is the projection operator that projects a Cartesian vector along the tangential directions $\hat{\theta}$ and $\hat{\phi}$ on S^2. This form of $\mathcal{P}$ is consistent in that the scattered far field $\vec{E}_s = [E_{s,\theta}, E_{s,\phi}]^T$ has no radial component and the same applies to the 2×2 matrix $\Phi_s = \langle \vec{E}_s^* \vec{E}_s^T \rangle$. Using Eq. (2), $\Re\{\Phi_s(\theta,\phi)\}$ is interpreted as the tangential projection from $\Re\{\Phi_f(x,y,z)\}$ along angle (θ,ϕ) on S^2.

Combining Eqs. (1) and (2), we have

$$D_0 \mathcal{P}(\theta,\phi) \Re\{\Phi_f(x,y,z)\} \mathcal{P}(\theta,\phi)^T = \frac{1}{2} s_0 I, \tag{3}$$

which determines the positions of the singularities on S^2 when the particle is moving.

These derivations have a clear geometric interpretation: The 3×3 real symmetric matrix for the focal fields $\Re\{\Phi_f(x,y,z)\}$ forms, geometrically, an (intensity) ellipsoid at each point in the focal plane [31]. The squared lengths of the ellipsoid's semiaxes (a^2, b^2, c^2, with $a^2 \geq b^2 \geq c^2$) are determined by the three independent focal intensity components I_x, I_y, and I_z, which can be obtained as the eigenvalues of $\Re\{\Phi_f(x,y,z)\}$ [31], as shown in the Supplemental Material [32]. Similarly, the 2×2 real symmetric matrix $\Re\{\Phi_s\}$ forms an ellipse. Equation (3) thus

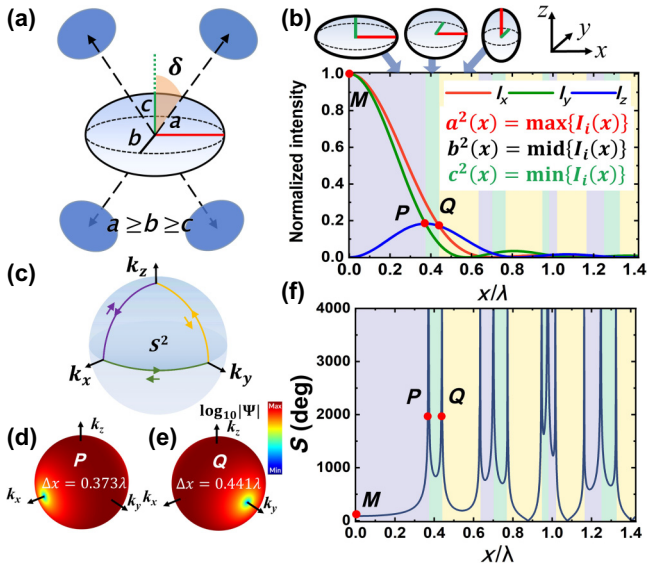

FIG. 2. (a) Directions of the four circular projections of an ellipsoid. (b) Normalized focal intensities with color-shaded regions corresponding to the same color-coded trajectory in (c). The top row shows the shape of the corresponding ellipsoid at different locations, with its longest and shortest axes represented by the red and green lines. (c) Trajectory of one singularity on S^2. (d, e) Locations of the singularities on S^2 when the particle is at points P and Q in (b). (f) Sensitivities at different positions, with the same color-coding scheme as (b).

interprets the angular positions of singularities on S^2 as directions, where the ellipsoid $\Re\{\Phi_f(x,y,z)\}$ projects into a circle. As the particle moves, the focal intensities at the particle's position vary. This changes the shape of the ellipsoid and, consequently, the directions of its circular projections on S^2. However, these circular projections persist, demonstrating the robustness of the scheme from a geometrical perspective.

In general, there are four circular projections of the ellipsoid, as shown in Fig. 2(a). They all lie in the plane spanned by the longest and shortest axes, $\hat{a}$ (red) and $\hat{c}$ (green), at an angle δ away from the $\hat{c}$ axis, with

$$\delta = \arctan\sqrt{\frac{a^2-b^2}{b^2-c^2}}. \tag{4}$$

Readers can find full explanations in the Supplemental Material [32]. This interpretation leads to a simple way to locate the singular points on S^2. For any incoming beam with its polarization matrix $\Phi_{\mathrm{in}} = \langle \vec{E}^*_{\mathrm{in}} \vec{E}^T_{\mathrm{in}} \rangle$ and $\vec{E}_{\mathrm{in}} = [E_{\mathrm{in},x}, E_{\mathrm{in},y}]^T$, one can obtain the independent focal intensity components (eigenvalues of $\Re\{\Phi_f\}$) via Richards-Wolf diffraction theory [29]. After reordering and substituting them into Eq. (4), the locations of the singular points are found.

B. Momentum-space dynamics of singularities and sensitivity analysis under unpolarized illumination

For unpolarized illumination, we have $\Phi_{\mathrm{in}} = \frac{1}{2}[1,0;0,1]$, where the 0s and 1s indicate uncorrelated incoming $E_{\mathrm{in},x}$ and $E_{\mathrm{in},y}$ components of equal intensity. Owing to the cylindrical symmetry of the focal field, it is sufficient to consider displacing the particle only along x. In Fig. 2(b), we plot the independent focal intensity components $I_x(x)$, $I_y(x)$, and $I_z(x)$ [29]. Their concrete forms, derived from Richards-Wolf theory, can be found in the Supplemental Material [32]. The associated ellipsoids are shown at the top, with the longest and shortest semiaxes marked in red and green, respectively. The shape of the ellipsoid changes at different x. Following Eq. (4), we obtain the corresponding trajectory of the singularities on S^2 in Fig. 2(c). Owing to symmetry, only the trajectory of one singularity is shown here; the complete dynamics can be found in the Supplemental Material [32]. Initially, at the north pole, when the particle is at $x = 0$, the singularity follows the purple, green, and yellow trajectories on S^2, corresponding to the particle's positions in the same color-shaded regions in Fig. 2(b).

Remarkably, between points P ($x = 0.373\lambda$) and Q ($x = 0.441\lambda$), a displacement of 0.068λ causes a 90° movement of the singularity on S^2 [Figs. 2(d) and 2(e)]. On average, a 1° change in this region can resolve a displacement of $7.6 \times 10^{-4}\lambda$. Considering the unpolarized illumination used, this sensitivity is very high.

To understand this, we define the local sensitivity $S = \mathrm{d}\delta/\mathrm{d}x_r$ as the angle $\mathrm{d}\delta$ swept by one singularity on S^2 per normalized displacement $\mathrm{d}x_r = \mathrm{d}x/\lambda$. Essentially, S is the geometric sensitivity related to the polarization state change at the focal plane, and can be obtained by taking the derivative of Eq. (4):

$$S(x_r) = \frac{(1-C)A' + (A-1)C'}{2(A-C)\sqrt{(A-1)(1-C)}}, \tag{5}$$

where we have used $A = a^2/b^2$ and $C = c^2/b^2$ to represent the normalized squared lengths of the ellipsoid and the prime denotes the derivative to the unitless normalized displacement x_r.

We plot S in Fig. 2(f); interestingly, for points at the boundaries of the shaded regions, S approaches infinity. These points correspond to the intersections of the two focal intensity curves shown in Fig. 2(b), with A or $C = 1$ and nonzero A' or C' satisfied in Eq. (5). We refer to them as points of infinite sensitivity (PISs). Around PISs, S is very high. There are generally two types of PIS; we can use point P and Q to explain their difference.

Around Q, we have intersections of I_x and I_z, as shown in Fig. 2(b). The ellipsoid has a circular cross section in the xz plane; thus, the singularities are along k_y, as shown in Fig. 2(e). Interestingly, the focal field at this PIS is circularly polarized in the xz plane. This is because both E_{fx}

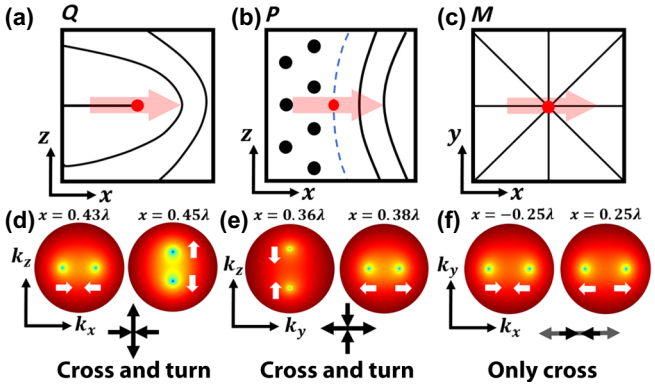

FIG. 3. (a–c) Major polarization axis distributions near (a) point Q, (b) point P, and (c) point M. The associated dynamics of the singular points on S^2 across these points, indicated by the red arrows, are shown in (d)–(f). At PISs, there is an abrupt change in the direction of the major axis and the singular points on S^2 show a crossing and 90° turning behavior, indicated by the white arrows on S^2 and black arrows at the bottom in (d) and (e).

and $E_{f,z}$ for the focal field are from the $E_{\text{in},x}$ component in the unpolarized incidence and are thus perfectly correlated with a phase difference of $\pi/2$, as shown in the Supplemental Material [32]. This is known as the transverse spin in the unpolarized focal field [25]. The singular points in Fig. 2(e) are thus circularly polarized. We refer to these Q-like points as type-I PISs. They originate from the spin part of the focal field and exist under both polarized and unpolarized illumination.

A similar analysis applies to point P; we have a PIS caused by the intersection of I_y and I_z. Unlike type-I PISs, $E_{f,y}$ and $E_{f,z}$ are from $E_{\text{in},y}$ and $E_{\text{in},x}$ components, separately, in the unpolarized incoming beam (see the Supplemental Material [32]). They are not correlated and the focal field is unpolarized in the yz plane. As a result, the singular points on S^2 along k_x in Fig. 2(d) are unpolarized. We refer to these P-like points as type-II PISs. They originate from the unpolarized part of the focal fields and are unique for unpolarized illumination.

The condition for a PIS is related to some unique polarization structures in the focal field and special dynamics on S^2. It is insightful to look at them in detail. In Figs. 3(a) and 3(b), we plot the major axis distribution near points P and Q. As stated before, the intensity ellipsoid has three independent axes, and we plot the major axis orientations inside the plane containing an almost circular cross section.

Across P and Q, there is an abrupt change in the direction of the in-plane major axis, as shown in Figs. 3(a) and 3(b). As a result of this axis jump, the trajectory of the singular points on S^2 shows a rapid crossing and 90° turning behavior in Figs. 3(d) and 3(e), within a displacement of 0.02λ. The formation of PISs at P and Q is closely related to the in-plane polarization singularity, with an abrupt change in the major axis direction.

As a comparison, we also look at point M, marked in Fig. 2(b), and the results are shown in Figs. 3(c) and 3(f). In contrast, the two intensity curves become tangential at M in Fig. 2(b), and we have a node-type structure in Fig. 3(c) around M. Although $A = 1$ is satisfied at M, there is no major axis jump across M along x, which makes $A' = 0$ as well. The two singular points on S^2 only cross each other and there is no 90° turning, as shown in Fig. 3(f). Thus, S remains finite around M; for a similar range of the angular movements of the singularities on S^2, as shown in Figs. 3(d)–3(f), the required x is 0.5λ around M, which is much larger than 0.02λ around P and Q.

We note that, in Fig. 2(f), the points P and Q are located very closely. The circular cross section of the ellipsoid quickly changes by 90° from the yz plane to the xz plane, owing to two subsequent intersections, of I_y, I_z at P and I_x, I_z at Q. This is because, in a tightly focused linearly polarized field, the focal spot is elongated along its direction of polarization. Therefore, as shown in Fig. 2(b), along x, I_x from $E_{\text{in},x}$ is elongated whereas I_y from $E_{\text{in},y}$ is not. Unlike polarized focal fields, as shown next, these two I_x and I_y curves exist independently, owing to incoherence, and only in this case do they both intersect with I_z, creating tightly spaced type-I and type-II PISs at a distance smaller than 0.1λ within the Airy disk. The very tight coexistence of type-I and type-II PISs is the key factor to increasing the overall sensitivity in neighboring regions, even in the presence of a noisy environment [32]. In such a case, the minimum resolved displacement remains finite, owing to experimental uncertainty. The coexistence of two PISs creates a broad range of high displacement sensitivity. This is a unique feature for unpolarized illumination; it results in a superior performance to that of the polarized case.

C. Comparison between polarized and unpolarized cases

Since our method is general, it applies to polarized illumination as well. For the polarized case, because the focal field is mostly elliptically polarized with only two independent focal intensities, the ellipsoid becomes an ellipse. The singular points then correspond to the circular projections of this ellipse. Setting $C = 0$, the PIS predicted by Eq. (5) because of the shape change of the ellipsoid still applies.

We then consider a polarized incidence described by $\Phi_{\text{in}} = 1/(1 + a_c)[1, \sqrt{a_c}i; -\sqrt{a_c}i, a_c]$, consisting of coherently related $E_{\text{in},x}$ and $E_{\text{in},y}$ components. Increasing a_c from 0 to 1, one increases the $E_{\text{in},y}$ component coherently to the entrance pupil, and the incoming polarization changes from linear to elliptical and circular. In particular, when $a_c = 1$, the incoming beam is circularly polarized. It has the same symmetry and intensity distributions at the entrance pupil and the focal plane as the unpolarized case. However, one is coherent and the other is incoherent.

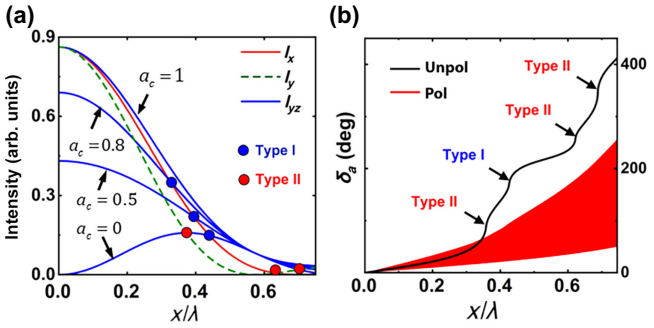

FIG. 4. (a) Focal intensities I_x (red) and I_{yz} (blue) for polarized illumination for different values of a_c; I_y is shown, for reference, as the dashed green line. Type-I and II PISs are marked as blue and red dots, respectively. (b) Accumulated angular shifts for the singular points, under unpolarized illumination (black curve) and for the polarized case with $a_c \in [0, 1]$ (red part).

Following the same procedure, we plot the focal intensities along x in Fig. 4(a) and look for PISs. This polarized focal field shares the same expressions for $I_x(x)$, $I_y(x)$, and $I_z(x)$ as the unpolarized case. However, because the field is polarized, the incoherent I_y curve shown as the dashed curve disappears. There are only two independent curves $I_{yz} = a_c I_y + I_z$ (blue) and I_x (red) left. They intersect only once within the Airy disk, marked as the blue dot. The focal field at this point is circularly polarized; thus, this is a type-I PIS, owing to spin. More specifically, when $a_c = 0$, the incident polarized beam has only the $E_{\text{in},x}$ component, and this point is exactly the same type-I PIS around Q for the unpolarized case. This type-I PIS comes solely from focusing of $E_{\text{in},x}$, either in a linearly polarized or an unpolarized incoming beam. As shown in Fig. 4(a), increasing $E_{\text{in},y}$ coherently makes the incoming polarization elliptical, and it only shifts I_{yz} upward and the type-I PIS inward. Surprisingly, coherence here decreases the number of PISs by making the type-II PIS marked with a red dot disappear. Even worse is that, when $a_c = 1$, the incoming beam is circularly polarized. As stated previously, it has the same focal intensity distributions as the unpolarized incidence and is the coherent counterpart of unpolarized illumination. In this case, the two curves I_x and I_{yz} become tangential at $x = 0$, as shown in Fig. 4(a). This means that $A = 1$ and $A' = 0$; this is similar to the point M discussed previously. According to Eq. (5), even the type-I PIS disappears, and there is no PIS under circularly polarized illumination.

It should be noted that, except for circular and unpolarized cases, all the other polarized focal fields have anisotropic 2D focal field distributions. Along the x-axis, most of the polarized cases have at least one type-I PIS, owing to spin; this is why we restrict the foregoing discussions to cases only along this axis. One can show that, for the 2D case, the total number of PISs within the Airy disk is 2 for the unpolarized case along all the directions, and at most 1 for the polarized case (circular polarization has no PIS). This makes the unpolarized case unique to all of these polarized cases. See the Supplemental Material [32] for two-dimensional distributions of PISs.

As the particle moves inside the focal field, the momentum-space singularities move on S^2 continuously and never disappear, owing to topological protection. One can track the singularity and calculate the accumulated spherical (angular) distances δ_a on S^2 for particle displacements from 0 to x under various types of illumination. This allows us to make a direct comparison between different kinds of illumination, as discussed in the foregoing. The results are shown in Fig. 4(b), where the black curve represents the unpolarized case and the densely packed red curves correspond to the polarized case for $a_c \in [0, 1]$; see the Supplemental Material [32] for a detailed expansion of the red part in Fig. 4(b). The two cases show similar δ_a before $x = 0.3\lambda$. At $x \in (0.35\lambda, 0.45\lambda)$, the unpolarized case has a significantly larger δ_a, owing to the coexistence of type-I and II PISs. In the presence of noise, this brings a broader range of high displacement sensitivity than polarized illumination [32]. Moving the particle further includes more type-II points. This makes δ_a for the unpolarized case even larger.

These discussions highlight some intriguing aspects of unpolarized light compared with its polarized counterpart, owing to its incoherent nature. In addition to the much less stringent requirement on phase or polarization stability, these aspects make the use of unpolarized illumination in displacement metrology particularly promising.

In the meantime, one also observes that the existence of the two types of PIS is closely related to the formation of the in-plane unpolarized or circularly polarized states (transverse spin), which are both highly robust against randomly fluctuating phases in quasimonochromatic unpolarized illumination. As we show in the following, the formation of these two closely packed PISs is even robust under broadband unpolarized illumination, and corresponds to the formation of circular cross sections of an effective broadband intensity ellipsoid.

D. Robustness under broadband illumination

To see this, we remove the restrictions of quasimonochromatic illumination and apply our method to the broadband case. To prove the existence of the topological singularities on S^2 under broadband illumination, we integrate Eq. (1) over the spectrum $f(\omega)$ on both sides [33], yielding

$$\Re\left\{\Phi_s^{\text{broad}}(\theta,\phi)\right\} = \frac{1}{2} s_0^{\text{broad}} I, \tag{6}$$

with $\Phi_s^{\text{broad}} = \int f(\omega)\Phi_s(\omega)\mathrm{d}\omega$ and $s_0^{\text{broad}} = \int f(\omega) s_0(\omega)\mathrm{d}\omega$. Since Eqs. (1) and (6) share the same structure, the

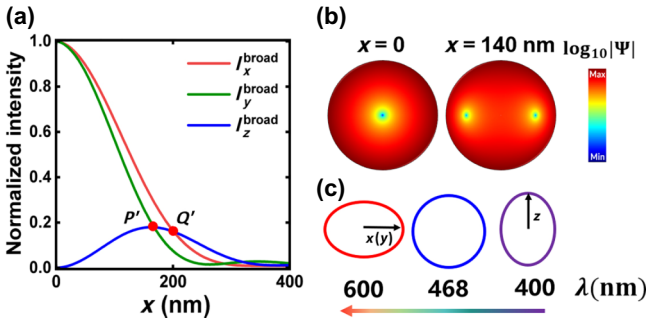

FIG. 5. (a) Squared lengths of the semiaxes for the broadband intensity ellipsoid. (b) Top view of locations of the broadband singularities at $x = 0$ nm and $x = 140$ nm on S^2. (c) Evolution of the polarization ellipse in the xz (yz) plane at point Q' (P') in the wavelength domain. Colors represent different wavelengths; the black arrows indicate the major axis orientation.

singularities still exist, and they correspond to the directions where $\Re\{\Phi_s^{\text{broad}}(\theta,\phi)\}$ has identical eigenvalues.

Under broadband unpolarized illumination, the same geometric interpretation holds, and the singular points are the circular projections of a broadband ellipsoid. However, the effective squared length of the semiaxis of the broadband ellipsoid should be modified, with

$$I_i^{\text{broad}} = \int f(\omega) D_0(\omega) \left(\frac{k^2 f^2}{4}\right) I_i \mathrm{d}\omega \tag{7}$$

for $i = x, y, z$. Here, I_i^{broad} is the sum of the monochromatic intensity component I_i weighted by the spectrum distribution $f(\omega)$, the scattering coefficient $D_0(\omega)$, and the focusing strength $k^2 f^2/4$. (See the Supplemental Material [32] for detailed derivations.)

In Fig. 5(a), we consider broadband unpolarized illumination covering 400 to 800 nm, with $f(\omega) = 1$. Following the same geometric interpretations, we plot I_x^{broad}, I_y^{broad}, and I_z^{broad}, representing the shape of the broadband ellipsoid. As x increases, the shape of the broadband ellipsoid varies, leading to splitting of the broadband singularities, as shown in Fig. 5(b). Interestingly, in Fig. 5(a), there are still points, for example at P' and Q', where the three curves intersect. Similar to points P and Q, discussed previously, they correspond to PISs.

To understand the robustness of the existence of these two points P' and Q' under broadband illumination, we recall that there is a position-wavelength equivalence in calculating the focal intensities in Fig. 2(b). Namely, there are two ways to change the normalized displacement $x_r = x/\lambda$: via x or via λ. For a quasimonochromatic illumination of a single wavelength λ, changing x leads to a change of in-plane major axis across points P and Q, as shown in Figs. 3(a) and 3(b). For the broadband case, at the same point x, varying λ from a broadband wavelength range effectively changes x_r. These two methods are equivalent. As a result, if one plots the in-plane major axis distribution at point P' or point Q', but in the wavelength domain, one can get similar patterns, as in Fig. 3(a) or Fig. 3(b); this is illustrated in Fig. 5(c). At 468 nm in the wavelength domain, the major in-plane axis is undefined and the field is unpolarized in the yz plane (P') or circularly polarized in the xz plane (Q'). Shorter or longer wavelengths correspond to elongated ellipses along orthogonal directions at the same position x. By averaging through the weighted sum given in Eq. (7), these ellipses average out, leaving one effective circular cross section, which exactly corresponds to points P' and Q' in Fig. 5(a) for the broadband case. The abrupt change of in-plane major axis in the wavelength domain in Fig. 5(c) ensures the robust existence of the two circular cross sections of the effective broadband ellipsoid, even under broadband illumination, whereas the abrupt change of the major in-plane axis of the effective broadband ellipsoid in the spatial domain in Figs. 3(a) and 3(b) is the main cause of PIS.

It is worth mentioning that the ellipse in Fig. 5(c) can also be interpreted as the polarization ellipse at different wavelengths observed at the singular point on S^2. However, because points P and Q have different natures, points P' and Q' inherit their properties. At point P', the singular points on S^2 are unpolarized at 468 nm, and they are partially polarized, with some linearly polarized components added, at shorter or longer wavelengths, as shown in Fig. 5(c). At Q', they are circularly polarized at 468 nm, and become elliptically polarized at shorter or longer wavelengths, with some linearly polarized components added.

III. EXTENSION AND CONCLUSION

Finally, we note that our method is based on topological protection in momentum space, which is required by the Poincaré-Hopf theorem. The Poincaré-Hopf theorem has no restrictions on the details of constructed vector or line fields; this generalizes our method. In addition to the line field, we construct a vector field $\vec{w} = \nabla_\perp s_2^{xy}$ on S^2, where s_2^{xy} is the Stokes parameter of the scattered far field, measured in Cartesian coordinates, and $\nabla_\perp$ is the transverse gradient operator. It can be shown that the index sum of $\vec{w}$ on S^2 is $+2$, as illustrated in the Supplemental Material [32]. There are three saddles on the upper hemisphere of S^2 in Fig. 6. Displacing the particle moves the two outermost saddles, first inward and then outward. The average sensitivity for each saddle point is approximately $13\,678^\circ/\lambda$, corresponding to a 1° resolvability of $7.3 \times 10^{-5}\lambda$.

In conclusion, using topological invariance, we propose a robust method for displacement metrology, even under broadband unpolarized illumination with randomly fluctuating phases. Surprisingly, these conventional sources of noise can enhance the displacement sensitivity by introducing an additional type-II PIS, owing to incoherence.

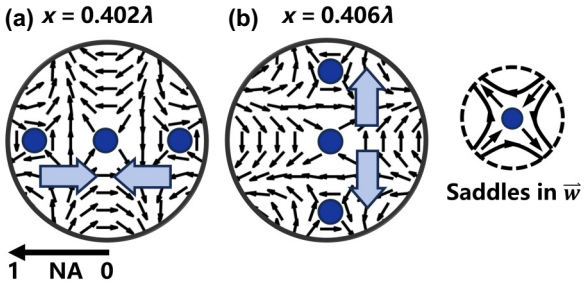

FIG. 6. Distributions of $\vec{w}$ (black arrows) on the upper hemisphere of S^2 at (a) $x = 0.402\lambda$ and (b) $x = 0.406\lambda$. The blue dots represent saddle point singularities with index -1, with more detailed topological structures shown on the far right. The blue arrows indicate the movement direction of the saddles. NA, numerical aperture.

Our work bridges the seemingly uncorrelated fields of topology and metrology, paving the way for the development of robust and ultrasensitive metrological schemes under conditions of randomly fluctuating sources.

ACKNOWLEDGMENTS

This work was supported by the National Key Research and Development Program of China (2021YFA1400700); the National Natural Science Foundation of China (Grant No. 62105320); the CAS Project for Young Scientists in Basic Research (Grant No. YSBR-049); and the Anhui Provincial Key Research and Development Project (202304a05020013).

DATA AVAILABILITY

The data that support the findings of this article are not publicly available. The data are available from the authors on reasonable request.

[1] P. J. De Groot, A review of selected topics in interferometric optical metrology, Rep. Progr. Phys. **82**, 056101 (2019).
[2] B. P. Abbott *et al.* (LIGO Scientific Collaboration and Virgo Collaboration) Observation of gravitational waves from a binary black hole merger, Phys. Rev. Lett. **116**, 061102 (2016).
[3] H. Deschout, F. C. Zanacchi, M. Mlodzianoski, A. Diaspro, J. Bewersdorf, S. T. Hess, and K. Braeckmans, Precisely and accurately localizing single emitters in fluorescence microscopy, Nat. Methods **11**, 253 (2014).
[4] R. G. Knobel and A. N. Cleland, Nanometre-scale displacement sensing using a single electron transistor, Nature **424**, 291 (2003).
[5] M. Krieg, G. Fläschner, D. Alsteens, B. M. Gaub, W. H. Roos, G. J. Wuite, H. E. Gaub, C. Gerber, Y. F. Dufrêne, and D. J. Müller, Atomic force microscopy-based mechanobiology, Nat. Rev. Phys. **1**, 41 (2019).
[6] F. Balzarotti, Y. Eilers, K. C. Gwosch, A. H. Gynnå, V. Westphal, F. D. Stefani, J. Elf, and S. W. Hell, Nanometer resolution imaging and tracking of fluorescent molecules with minimal photon fluxes, Science **355**, 606 (2017).
[7] B. Abbott, R. Abbott, R. Adhikari, P. Ajith, B. Allen, G. Allen, R. Amin, S. Anderson, W. Anderson, M. Arain, *et al.*, LIGO: The laser interferometer gravitational-wave observatory, Rep. Progr. Phys. **72**, 076901 (2009).
[8] M. Aspelmeyer, T. J. Kippenberg, and F. Marquardt, Cavity optomechanics, Rev. Mod. Phys. **86**, 1391 (2014).
[9] V. Giovannetti, S. Lloyd, and L. Maccone, Quantum-enhanced measurements: Beating the standard quantum limit, Science **306**, 1330 (2004).
[10] R. Barboza, A. Babazadeh, L. Marrucci, F. Cardano, C. de Lisio, and V. D'Ambrosio, Ultra-sensitive measurement of transverse displacements with linear photonic gears, Nat. Commun. **13**, 1080 (2022).
[11] M. Neugebauer, P. Woźniak, A. Bag, G. Leuchs, and P. Banzer, Polarization-controlled directional scattering for nanoscopic position sensing, Nat. Commun. **7**, 11286 (2016).
[12] Z. Xi, L. Wei, A. J. L. Adam, H. P. Urbach, and L. Du, Accurate feeding of nanoantenna by singular optics for nanoscale translational and rotational displacement sensing, Phys. Rev. Lett. **117**, 113903 (2016).
[13] A. Bag, M. Neugebauer, P. Woźniak, G. Leuchs, and P. Banzer, Transverse Kerker scattering for angstrom localization of nanoparticles, Phys. Rev. Lett. **121**, 193902 (2018).
[14] D. S. Simon, *Topology in Optics: Tying Light in Knots* (Morgan & Claypool Publishers, San Rafael, CA, 2021).
[15] M. Z. Hasan and C. L. Kane, Colloquium: Topological insulators, Rev. Mod. Phys. **82**, 3045 (2010).
[16] T. Ozawa, H. M. Price, A. Amo, N. Goldman, M. Hafezi, L. Lu, M. C. Rechtsman, D. Schuster, J. Simon, O. Zilberberg, *et al.*, Topological photonics, Rev. Mod. Phys. **91**, 015006 (2019).
[17] B. Zhen, C. W. Hsu, L. Lu, A. D. Stone, and M. Soljačić, Topological nature of optical bound states in the continuum, Phys. Rev. Lett. **113**, 257401 (2014).
[18] J. Jin, X. Yin, L. Ni, M. Soljačić, B. Zhen, and C. Peng, Topologically enabled ultrahigh-Q guided resonances robust to out-of-plane scattering, Nature **574**, 501 (2019).
[19] X. Yin, J. Jin, M. Soljačić, C. Peng, and B. Zhen, Observation of topologically enabled unidirectional guided resonances, Nature **580**, 467 (2020).
[20] A. B. Khanikaev and A. Alù, Topological photonics: Robustness and beyond, Nat. Commun. **15**, 931 (2024).
[21] H. Hopf, *Differential Geometry in the Large: Seminar Lectures New York University 1946 and Stanford University 1956* (Springer, Berlin, 2013), Vol. 1000.
[22] G. J. Gbur, *Singular Optics* (CRC Press, Boca Raton, FL, 2016).
[23] L. Mandel and E. Wolf, *Optical Coherence and Quantum Optics* (Cambridge University Press, Cambridge, U.K., 1995).
[24] K. Lindfors, A. Priimagi, T. Setälä, A. Shevchenko, A. T. Friberg, and M. Kaivola, Local polarization of tightly focused unpolarized light, Nat. Photonics **1**, 228 (2007).

[25] J. Eismann, L. Nicholls, D. Roth, M. A. Alonso, P. Banzer, F. Rodríguez-Fortuño, A. Zayats, F. Nori, and K. Bliokh, Transverse spinning of unpolarized light, Nat. Photonics **15**, 156 (2021).

[26] J. S. Eismann, *Dipoles in Nanooptics: From Their Tailored Excitation to a Nanoscopic Measurement Tool* (Friedrich-Alexander-Universitaet Erlangen-Nuernberg, Germany, 2023).

[27] M. Berry, M. Dennis, and R. Lee, Polarization singularities in the clear sky, New J. Phys. **6**, 162 (2004).

[28] M. S. Soskin, V. Denisenko, and I. Freund, Optical polarization singularities and elliptic stationary points, Opt. Lett. **28**, 1475 (2003).

[29] K. Lindfors, T. Setälä, M. Kaivola, and A. T. Friberg, Degree of polarization in tightly focused optical fields, J. Opt. Soc. Am. A **22**, 561 (2005).

[30] L.-P. Leppänen, A. T. Friberg, and T. Setälä, Partial polarization of optical beams and near fields probed with a nanoscatterer, J. Opt. Soc. Am. A **31**, 1627 (2014).

[31] M. Dennis, Geometric interpretation of the three-dimensional coherence matrix for nonparaxial polarization, J. Opt. A: Pure Appl. Opt. **6**, S26 (2004).

[32] See Supplemental Material at http://link.aps.org/supplemental/10.1103/q77s-h3wg for a detailed description of the derivation of the polarization matrix, dynamics of the singularities on S^2, positions of the circular projections, lengths of the semiaxes for the broadband ellipsoid, and distributions of $\vec{w}$ on S^2, as well as a detailed sensitivity analysis.

[33] C. Brosseau, *Fundamentals of Polarized Light: A Statistical Optics Approach* (John Wiley & Sons, Inc., New York, 1998).